catalysts

MDPI

Article

Structural Effects of Microcrystalline Cellulose-Derived Carbon Supports on Catalytic Performance of the $Pd(OH)_2/C$ Catalysts for the Hydrogenolytic Debenzylation of Hexanitrohexaazaisowurtzitane Derivatives

Yuling Wang [1], Yun Chen [2], Xinlei Ding [1], Jianwei Song [3], Gaixia Wei [3], Hengwei Dai [1], Hanyang Wang [1], Yadong Liu [1], Guangmei Bai [1] and Wenge Qiu [1,*]

[1] Beijing Key Laboratory for Green Catalysis and Separation, Faculty of Environmental and Life, Beijing University of Technology, Beijing 100124, China
[2] School of Chemistry and Chemical Engineering, Beijing Institute of Technology, Beijing 100081, China
[3] Qing Yang Chemical Industry Corporation, Liaoyang 111001, China
* Correspondence: qiuwenge@bjut.edu.cn

Abstract: In order to reduce the noble metal palladium dosage in the preparation of CL-20 so as to reduce its production cost, several carbon supports were prepared successfully using the hydrothermal carbonization method in the absence or presence of urea using microcrystalline cellulose (MC) as the carbon source, and the corresponding $Pd(OH)_2/C$ catalysts were fabricated using the deposition–precipitation method, which showed high activity in the debenzylation reaction of hexabenzylhexaazaisowurtzitane (HBIW) and tetraacetyldibenzylhexaazaisowurtzitane (TADB). It was found that all the catalysts showed a high efficiency in the debenzylation of HBIW, indicating that the structure of the used carbon supports had a limited impact on the catalyst performance in this reaction. On the contrary, the activities of the catalysts in the debenzylation of TADB were quite different. The results of the nitrogen sorption isotherm measurement (BET), scanning electron microscope (SEM), scanning transmission electron microscopy (STEM), powder X-ray diffraction (XRD), element analysis and temperature programmed desorption (TPD), as well as X-ray photoelectron spectra (XPS) characterizations of the supports and catalysts, showed that the relatively high activity of Pd/HTC in the debenzylation of TADB was related to the high Pd dispersion and novel mesoporous structure, while the further higher activity and stability of Pd/HTC-$N_{1:1}$ in the same reaction were related with its high Pd dispersion, high total oxidized Pd species, and high surface pyridinic N contents as well as the eggshell distribution of Pd species on the support.

Keywords: nitrogen doping carbon support; $Pd(OH)_2/C$ catalyst; hydrogenolytic debenzylation

Citation: Wang, Y.; Chen, Y.; Ding, X.; Song, J.; Wei, G.; Dai, H.; Wang, H.; Liu, Y.; Bai, G.; Qiu, W. Structural Effects of Microcrystalline Cellulose-Derived Carbon Supports on Catalytic Performance of the $Pd(OH)_2/C$ Catalysts for the Hydrogenolytic Debenzylation of Hexanitrohexaazaisowurtzitane Derivatives. *Catalysts* **2023**, *13*, 637. https://doi.org/10.3390/catal13030637

Academic Editors: Hongxing Dai, Xiang Wang, Yujun Zhu, Haibao Huang and Yunkun Zhao

Received: 28 February 2023
Revised: 16 March 2023
Accepted: 21 March 2023
Published: 22 March 2023

1. Introduction

The benzyl group has been one of the most broadly employed protecting groups for O- and N-based functionalities in fine chemical synthesis and organic transformations [1]. The introduction of the benzyl group is usually easier, but its removal is sometimes a thorny problem, especially for the removal of a few N-benzyl groups. The reported benzyl removal methods included a direct catalytic hydrogenation with H_2 [2,3], transfer hydrogenation with $NaBH_4$ or ammonium formate [4,5], acid catalysis using $AlCl_3$ or triflic acid [6,7], etc. Among them, Pd/C or $Pd(OH)_2/C$ catalyzed hydrogenolysis for N-debenzylation using H_2 has been the most commonly used one due to its high efficiency, atom economy, and easy-to-recycle active component [8]. Hexabenzylhexaazaisowurtzitane (HBIW) was an important precursor for the synthesis of hexanitrohexaazaisowurtzitane (HNIW or CL-20, Scheme 1) [9–11], one of the most important molecules in high-energy-density materials' area, hence the hydrogenolytic debenzylation of HBIW and tetraacetyldibenzylhexaazaisowurtzitane (TADB) became a key step for the fabrication of CL-20 [12,13]. However,

this step needs to be carried out under mild conditions due to the relatively low stability of the hexanitrohexaazaisowurtzitane cage skeleton. There is an urgent requirement to develop catalysts with a high efficiency at near room temperature to meet the catalytic transformation of HBIW.

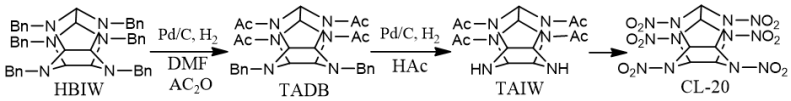

Scheme 1. Synthetic route of CL-20.

In the past decades, several efficient catalysts, such as $Pd(OH)_2$ nanoparticles [14], Pd/C [15–17], $Pd(OH)_2/C$ [18–23], Pd/TiO_2 [24,25], Pd/DOWEX [26], Pd/mpg-C_3N_4 [27], and PdFe bimetallic catalysts [28,29] have been reported except the traditional commercial Pearlman catalyst and Degussa E101 NE/W [10,11]. It is well known that the textural and surface chemical properties of carbon carrier have significant effects on the catalytic performance of palladium-based catalysts, which influenced not only the Pd dispersion, particle size, and morphology, as well as the electronic structure of Pd species, but also the adsorption and diffusion of substrate and product molecules in the catalyst framework [30,31]. In this regard, there is a growing need to develop novel carbon supports that are suitable for the preparation of high-efficiency Pd/C or $Pd(OH)_2/C$ catalysts. In recent years, biomass-based carbon materials have attracted much attention due to their cheap, renewable, and abundant raw materials source [32,33]. Cellulose is the main component of biomass, which makes up 40–60 wt% of plant cell wall besides hemicellulose and lignin. In the past decade, many cellulose-derived porous carbons have been prepared from cellulose nanocrystals [34–36], nanofibrils [37], and bacterial nanocellulose [38,39] as well as microcrystalline cellulose (MC) [40–46]. Among them, MC was a cheaper and more readily available substrate. In terms of cost and sustainable development, MC was considered a promising carbon precursor, and several MC-derived carbon materials have also been reported for their electrode materials [41,44] and catalyst supports [43] due to their easy structure regulation. In addition, hydrothermal carbonization has been demonstrated as an effective way for biochar production, commonly named hydrochar. Moreover, hydrochar has a relatively lower ash content and higher C recovery compared to the biochar produced by traditional pyrolysis or gasification [47]. In this work, a series of carbon supports were fabricated using the hydrothermal carbonization method in the absence or presence of urea using MC as the carbon source, and the corresponding $Pd(OH)_2/C$ catalysts were prepared using a traditional deposition–precipitation method, which showed a high activity in the debenzylation reaction of HBIW and TADB, particularly, the Pd/HTC-$N_{1:1}$. The high activity and stability of Pd/HTC-$N_{1:1}$ were related to its high Pd dispersion, high total oxidized Pd species, and high surface pyridinic N contents as well as the eggshell distribution of Pd species on the support.

2. Results and Discussion

2.1. Synthesis and Characterization of the Carbon Supports

Five carbon supports were prepared using a hydrothermal method in the absence or presence of urea using MC as the carbon source. The SEM images of the carbon samples were summarized in Figure 1. For all the carbon samples, a lot of carbon microspheres were produced on the surface of their main blocky skeletons due to the hydrothermal conversion of cellulose [48]. However, the microsphere radiuses of HTC-N_x were much larger than that of HTC due to the condensation reaction between glucose and urea molecules in the hydrothermal process, leading to the formation of a large carbon nucleus, revealing the influence of nitrogen doping on the hydrothermal process of MC.

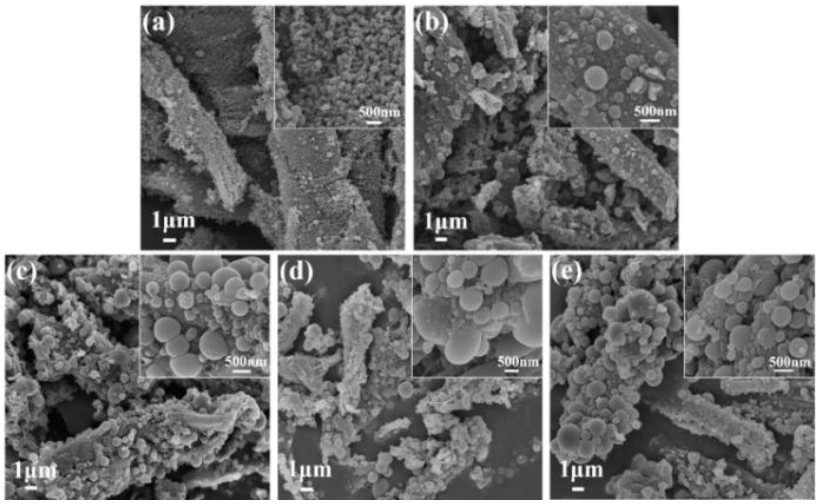

Figure 1. SEM images of the samples of HTC (**a**), HTC-$N_{3:1}$ (**b**), HTC-$N_{2:1}$ (**c**), HTC-$N_{1:1}$ (**d**), and HTC-$N_{1:2}$ (**e**).

The N_2 adsorption–desorption isotherms and the pore size distributions of the carbon supports are shown in Figure 2, while the BET surface areas and textural properties are summarized in Table 1. The HTC sample showed a type IV nitrogen adsorption isotherm and a H3 type hysteresis loop, indicating the existence of meso- and macro-pores within the carbon skeleton. The relatively high total surface area (449 m^2/g) and micropores surface area (334 m^2/g) of HTC demonstrated a porous structure. The shape of the adsorption isotherm of HTC-$N_{1:1}$ was similar to that of HTC, but its N_2 adsorption amount and surface area were much lower compared to HTC (Table 1), which could be attributed to the decrease in the micropore ratio, implying that nitrogen doping inhibited significantly the formation of micropores. For HTC-$N_{3:1}$, HTC-$N_{2:1}$, and HTC-$N_{1:2}$ (Figure S1), this inhibition phenomenon is more obvious, and their surface areas were lower than 10 m^2/g, inferring their deficient micropore structures. The pore-size distribution curves and the significant differences of pore volumes further demonstrated the porous structure of HTC and the low porosity of and HTC-N_x (Figure 2b). The relatively large pore width (6.6–9.5 nm) suggested the existence of piled mesopores.

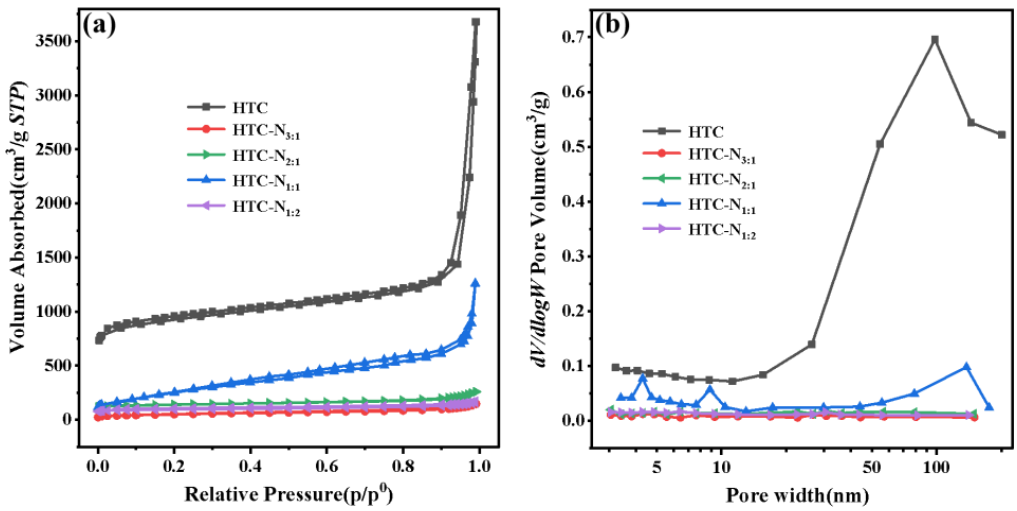

Figure 2. N_2 absorption–desorption isotherms (**a**) and pore-size distribution curves of the carbon supports (**b**).

Table 1. Textural and structural properties of the carbon supports.

Sample	S_{BET} ($m^2 \cdot g^{-1}$)	S_{mic} ($m^2 \cdot g^{-1}$)	V_{tot} ($m^2 \cdot g^{-1}$)	Average Pore Width (nm)
HTC	449.0	334.0	0.735	6.6
HTC-$N_{3:1}$	9.3	0.0	0.016	7.0
HTC-$N_{2:1}$	9.2	0.6	0.018	7.7
HTC-$N_{1:1}$	35.0	0.0	0.083	9.5
HTC-$N_{1:2}$	9.9	0.0	0.018	7.3

The crystalline structures of the carbon carriers were characterized by XRD (Figure S2). The presence of a broad diffraction peak and a weak peak at around 2θ = 23° and 44° corresponding to the (002) and (100) diffractions of graphitic carbon (JCPDS No. 41-1487) revealed the main amorphous structure and the relatively low degree of graphitization of these carbon samples [49]. The diffraction peak positions of the (002) crystal face of the HTC-N_x samples shifted slightly to the higher angle range than that of HTC, which could be attributed to the shrinkage of the carbon–carbon layer space due to the nitrogen atom doping [50]. Raman spectra were also used to investigate the graphitization degree of the received carbon samples (Figure S3). Two well-defined bands centered at 1350 and 1590 cm^{-1} were observed, known as the D and G bands, corresponding to the disordered carbon (associated with defects) and ordered carbon (related to graphitic carbon), respectively [51]. Compared with HTC, the G peak of the HTC-N_x samples presented evidently a red shift to 1570 cm^{-1}, indicating a higher disorder in the carbon skeleton of HTC-N_x [52]. The intensity ratio of the D and G band (I_D/I_G) was also an indicator of the level of graphitic degree of carbon materials. The I_D/I_G ratio of the HTC-N_x samples were slightly higher than that of HTC, further demonstrating that there were more defects in the HTC-N_x skeleton due to nitrogen doping, which led to the disorder of the carbon matrix and the increase in defect sites. The chemical compositions of the carbon supports are listed in Table 2. The HTC sample had a negligibly low N content of 0.3 wt%, which was due to pyrolyzation under a N_2 atmosphere, while the HTC-N_x samples possessed much higher N contents from 7.6 to 9.6 wt%. The N contents of the resulting carbon were lower compared to that of the actual urea doses, and this could be attributed to the direct decomposition of partial urea molecules before the hydrothermal reaction and the removal of partial-nitrogen-containing groups in the calcination process. As expected, the N contents of the carbon support increased as the initial urea quantity. Meanwhile, the O contents of carbon samples also increased gradually in the same order, revealing that some oxygen functional groups were introduced at the same time.

Table 2. Elementary compositions of the carbon samples.

Samples	Elemental Analysis (wt%)			
	N	C	H	O
HTC	0.3	91.3	1.8	6.6
HTC-$N_{3:1}$	7.6	82.6	1.4	8.4
HTC-$N_{2:1}$	8.2	81.9	1.2	8.7
HTC-$N_{1:1}$	8.8	80.9	1.4	8.9
HTC-$N_{1:2}$	9.6	77.0	1.3	12.1

To further insight the surface chemical properties of the carbon carriers, the temperature programmed desorption (TPD) was carried out under an inert atmosphere. The TPD patterns of the carbon supports are presented in Figure 3. For the HTC sample, there was a distinct CO_2 desorption peak at the temperature range of 150–650 °C, which was attributed to the decomposition of carboxylic acid and anhydride groups [53], while the four HTC-N_x samples had two CO_2 desorption peaks at 150–400 °C and 700–900 °C, which could be assigned to the decomposition of carboxylic acid/anhydride groups and stable lactone

groups [53]. Figure 4b displays the CO spectra of the carbon supports. The CO desorption curves of the carbon materials were similar. Distinct signals were detected at above 700 °C, which could be attributed to the decomposition of high stable phenol and quinonoid groups [54]. The TPD data further revealed the difference in the oxygen-containing groups and their distributions on HTC and HTC-N_x.

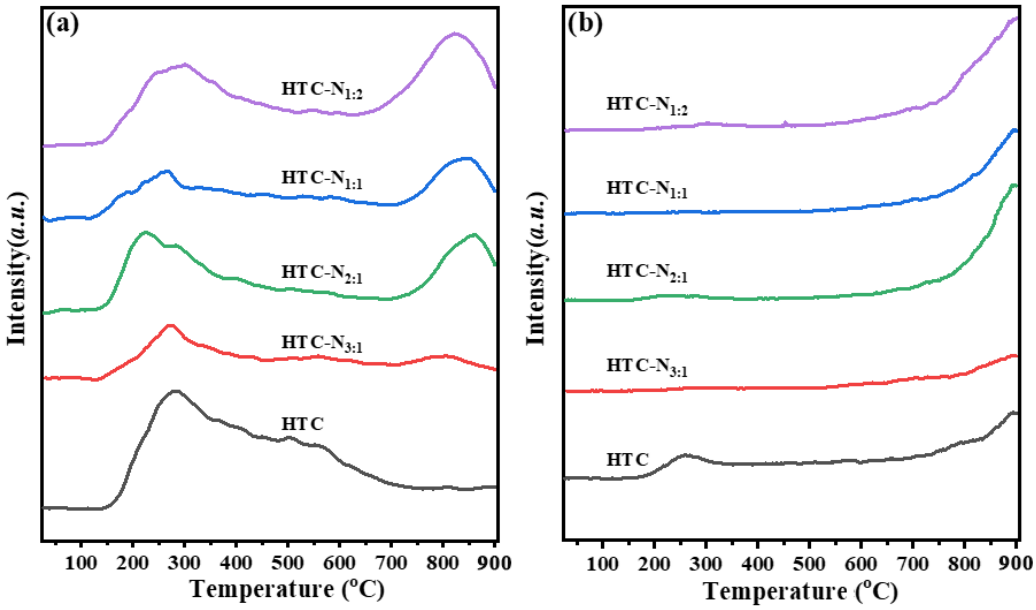

Figure 3. CO_2-TPD (**a**) and CO-TPD (**b**) profiles of the resultant carbon supports.

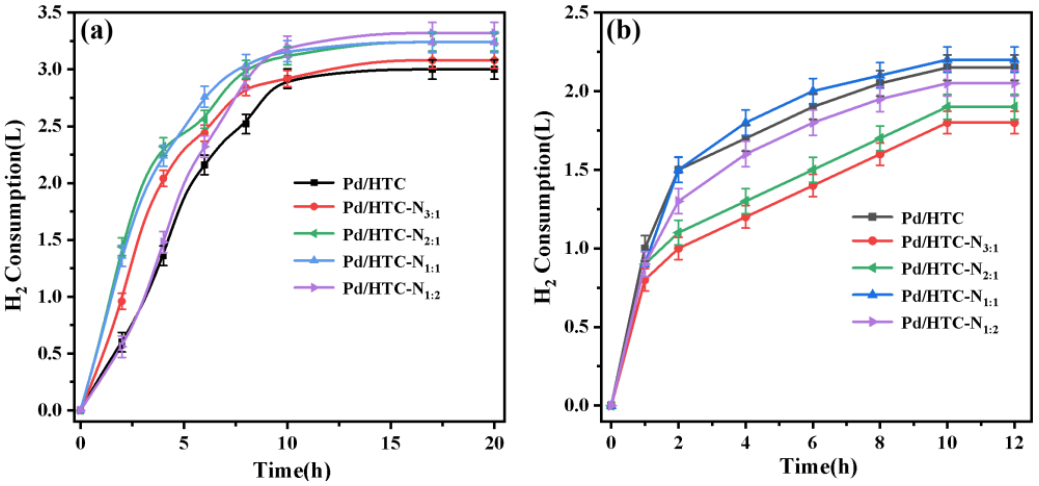

Figure 4. Hydrogen consumption amounts as functions of reaction times during the hydrogenolysis reaction of HBIW (**a**) and TADB (**b**) over various catalysts.

2.2. Catalytic Performance Characterization of the Catalysts

A series of $Pd(OH)_2/C$ catalysts were prepared by traditional deposition–precipitation method using the above mentioned carbon materials as supports (Scheme 2). The catalytic activities and the hydrogen consumption amounts as a function of the reaction times in the hydrogenolytic debenzylation reaction of HBIW and TADB are shown in Table 3 and Figure 4, respectively. It was found that the hydrogen consumption rates over the catalysts were fast in the earlier reaction stage (0–5 h), and then decreased gradually in the debenzylation of HBIW, which was similar to the reported reaction process [17]. Pd/HTC-$N_{1:1}$ and Pd/HTC-$N_{2:1}$, that had middle nitrogen contents in their supports, showed slightly faster reaction rates in the first 5 h than the other catalysts, indicating the

slight difference in their catalytic activity. However, all the TADB yields of the various catalysts were high (Table 3), demonstrating that all the catalysts were highly efficient in the debenzylation reaction of HBIW. These activities were much better than the most reported catalysts, such as Pd/ST-2.5, Pd/mpg-C_3N_4, and Pd_5Fe_1/Si-CODP, and comparable to Pd/TiO_2-2 (Table 4). It was known that the removal of benzyl groups in TADB molecule required a relatively more stringent condition compared to HBIW [21,26], in which an acid assistant was commonly needed, thus TADB was a better substrate to evaluate the catalyst activity. The kinetic curves clearly showed that the hydrogen consumption rates of the catalysts decreased in different degrees after the first hour (Figure 4b), indicating the difference in the activity and stability, which was also reflected in the hydrogen reaction amounts. The total hydrogen consumption amount of Pd/HTC-$N_{1:1}$ within 12 h was similar to that of Pd/HTC, which was higher than that of the other catalysts. The TADB conversions of the catalysts were in the order of Pd/HTC-$N_{1:1}$ > Pd/HTC > Pd/HTC-$N_{1:2}$ > Pd/HTC-$N_{2:1}$ > Pd/HTC-$N_{3:1}$, which was consistent with the total hydrogen consumption amounts, indicating the difference in the activity. For Pd/HTC-$N_{1:1}$, when the Pd dosage increased from 2.0 ‰ to 2.35 ‰, a TADB complete conversion could be realized stably (Table 3 entry 4). This was the lowest Pd dosage for the debenzylation reaction of TADB compared to the reported catalysts (Table 4) [22,24,26–28]. For the reported Pd/TiO_2-2 and Pd_5Fe_1/Si-CODP catalysts, 4.0% and 10.0% Pd dosages were needed to attain TADB complete conversion (Table 4 number 2 and 4). Considering the similar reaction condition, it implied that Pd/HTC-$N_{1:1}$ showed a much high activity in the TADB debenzylation. The result was useful to reduce the consumption of precious metal palladium and the production cost of CL-20.

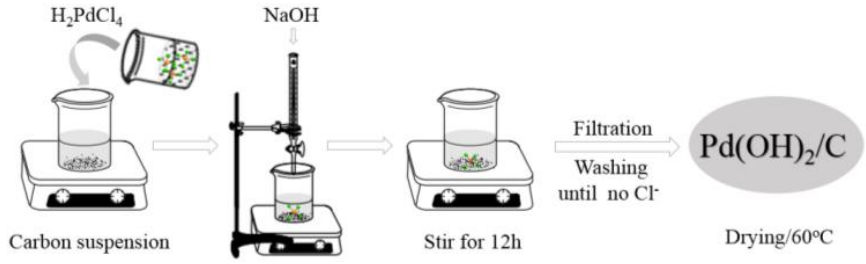

Scheme 2. Process of catalyst preparation.

Table 3. Activities of the catalysts in the debenzylation reactions of HBIW and TADB.

Number	Catalysts	Pd/Substrate (‰)		Results (%)	
		Pd/HBIW	Pd/TADB	TADB Yields	TADB Conversions
1	Pd/HTC	1.4	2.0	90	94
2	Pd/HTC-$N_{3:1}$	1.4	2.0	89	64
3	Pd/HTC-$N_{2:1}$	1.4	2.0	89	75
4	Pd/HTC-$N_{1:1}$	1.4	2.0/2.35	90	97/100
5	Pd/HTC-$N_{1:2}$	1.4	2.0	89	88

In order to further understand the effect of the nitrogen doping of a carbon support on the catalytic performance of the $Pd(OH)_2$/C catalysts, the recycling experiments of Pd/HTC and Pd/HTC-$N_{1:1}$ in the debenzylation of TADB were performed under an identical condition, and the recovered catalyst was used for the next reaction run after filtration without any further purification. Figure 5 presents the hydrogen consumption curves as a function of time over Pd/HTC and Pd/HTC-$N_{1:1}$ during the three cycles. For the Pd/HTC catalyst, the hydrogen consumption rate decreased obviously in the recycling experiments, and the TADB conversions in the second and third runs decreased to 76% and 56%, respectively (Table S1). On the contrary, the hydrogen consumption rate of Pd/HTC-$N_{1:1}$ in the second run was comparable to the first run, and the substrate still

realized the full conversion. Moreover, the TADB conversion in the third run was still up to 86%. The result indicated that the introduction of nitrogen into the carbon matrix enhanced significantly the stability of the corresponding $Pd(OH)_2/C$ catalyst due to the strong interaction between Pd and N atoms on the carbon carrier surface.

Table 4. Comparison of the catalyst's activities in the debenzylation reactions of HBIW and TADB.

No.	Catalysts	Pd/Substrate (‰)		Results (%)		Ref.
		Pd/HBIW	Pd/TADB	TADB Yields	TADB Conversions/TAIW Yields	
1	Pd/ST-2.5	7.0	-	82	-	[24]
2	Pd/TiO_2-2	1.0	4.0	89	100/88	[25]
3	Pd/mpg-C_3N_4	10.0	-	81.7	-	[27]
4	Pd_5Fe_1/Si-CODP	4.0	10.0	79	100/84	[29]
5	Pd/HTC	1.4	2.0	90	94/81	this work
6	Pd/HTC-$N_{1:1}$	1.4	2.0//2.35	90	97/82//100/87	this work

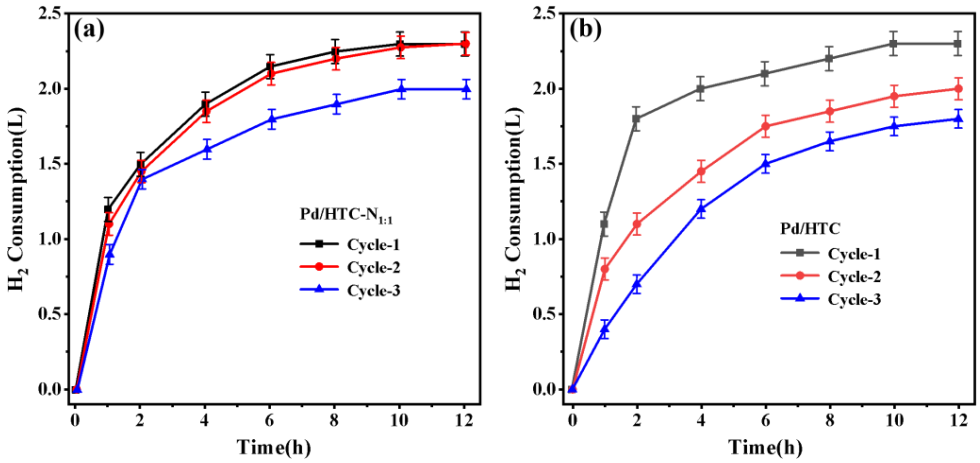

Figure 5. Hydrogen consumption amounts as functions of time during the hydrogenolysis reaction of TADB over Pd/HTC (**a**) and Pd/HTC-$N_{1:1}$ (**b**) catalysts in the cycling experiments.

2.3. Characterization of the Catalysts

The XRD patterns of different catalysts are shown in Figure 6. Compared to the XRD data of carbon supports (Figure S2), one additional weak and wide peak at around 34° could be observed for all the catalysts, which was attributed to the PdO species, indicating a high Pd dispersion and the main existing form of Pd. However, for Pd/HTC, three sharp peaks at 2θ of ~40, 46, and 68° could also be found, which were assigned to the (111), (200), and (220) diffractions of the Pd^0 species, respectively, demonstrating the present of a few crystal Pd^0 particles on its surface [55]. While the Pd^0 signal on the Pd/HTC-N_x catalysts was much weaker, implying the low ratio of the Pd^0 species or an amorphous structure.

To obtain the dispersion information of Pd species, STEM analysis was conducted. The STEM images and the Pd particle size distribution of the catalysts are shown in Figure 7. As Figure 7a,g show, the palladium species were well dispersed on Pd/HTC and Pd/HTC-$N_{1:1}$, in which most Pd particles were less than 3 nm and their average particle sizes were 2.83 nm and 2.55 nm, respectively. The Pd average particle sizes of Pd/HTC-$N_{1:1}$ was even smaller than that of Pd/HTC. Combining the large difference in the surface areas between HTC and HTC-$N_{1:1}$ (Table 1), it indicated that the introduction of the N atom into the carbon matrix was instructive to improve the Pd dispersion due to the interaction between Pd and N atoms. The elemental mappings of carbon (C), oxygen (O), nitrogen (N), and palladium (Pd) in Pd/HTC-$N_{1:1}$ further revealed the uniform distribution of Pd, O, and N atoms over the entire carbon skeleton (Figure 7k,l). For the Pd/HTC-$N_{3:1}$, Pd/HTC-$N_{2:1}$,

and Pd/HTC-$N_{1:2}$ catalysts, their statistical average particle sizes of Pd particles were 3.43 nm, 3.41 nm, and 3.11 nm, respectively, but a few aggregates larger than 6 nm could be observed clearly in the images, showing the decline of Pd dispersion on them. It could be attributed to the much low specific surface areas of the three carbon supports. The average Pd particle sizes of the five catalysts were in the order of Pd/HTC-$N_{1:1}$ > Pd/HTC > Pd/HTC-$N_{1:2}$ > Pd/HTC-$N_{2:1}$ > Pd/HTC-$N_{3:1}$, which was consistent with their activities in the debenzylation of TADB, revealing that the Pd dispersion might be a main reason as to why the catalyst activity was affected. In addition, the low specific surface area and lack of micropores of the nitrogen doping carbon led to the Pd/HTC-N_x catalyst with an eggshell distribution of Pd species on the support (Figure S4). It was also favorable to the catalytic debenzylation reaction. The relatively strong diffraction signal of Pd^0 species in the SAED pattern revealed a higher Pd^0 density in microregion within Pd/HTC-$N_{1:1}$ compared to Pd/HTC (Figure 7a,g insets), which was in accordance with the eggshell distribution of the Pd species.

The SEM images of the recovered Pd/HTC and Pd/HTC-$N_{1:1}$ samples after three cycles in the hydrogenolysis reaction of TADB indicated that there was no obvious change in catalyst morphology (Figure S5). The STEM images of the recovered Pd/HTC and Pd/HTC-$N_{1:1}$ as well as the histograms of Pd particle size distribution of the samples showed the growth of Pd particles in a certain degree due to the aggregation of Pd species in the reaction (Figure S6). This might be one reason for the deactivated the catalysts. However, the growths of the Pd particle size of Pd/HTC and Pd/HTC-$N_{1:1}$ were quite different. The change in the Pd size of Pd/HTC-$N_{1:1}$ (2.55 to 3.04 nm) was much lower than that of Pd/HTC (2.83 to 4.16 nm), suggesting that the aggregation of Pd species in the reaction was significantly inhibited due to the relatively strong interaction between Pd and N atoms on the carbon matrix.

To insight the surface composition and chemical states of the catalysts, XPS analysis was performed, and the XPS survey spectra corroborated the existence of Pd, C, N, and O in the catalysts (Figure S7). The surface atomic concentrations of Pd, N, O, and C were determined using the Peak-Fit program (Table S2). The order of the surface N concentrations was in agreement with the total N contents of the nitrogen-containing catalysts. Meanwhile, the order of the surface Pd concentrations was consistent with the surface O concentrations, which further demonstrated the main PdO form of Pd species on the catalyst surface. The large difference in the concentrations of surface Pd from 1.55% of Pd/HTC to 7.66% of Pd/HTC-$N_{2:1}$ might be related to the different surface areas and surface-oxygen-containing and nitrogen-containing groups' concentrations.

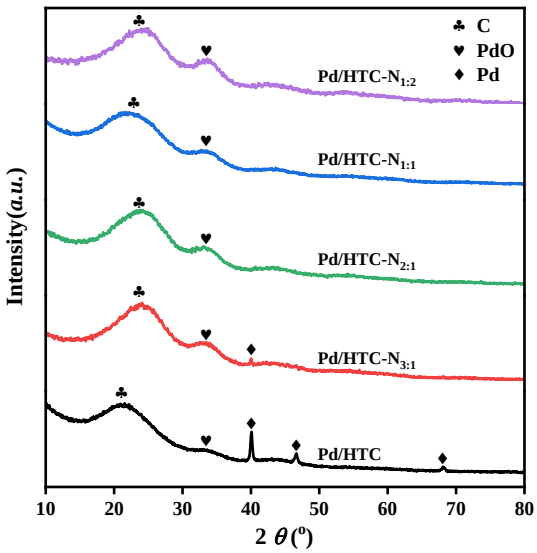

Figure 6. XRD patterns of the different catalysts.

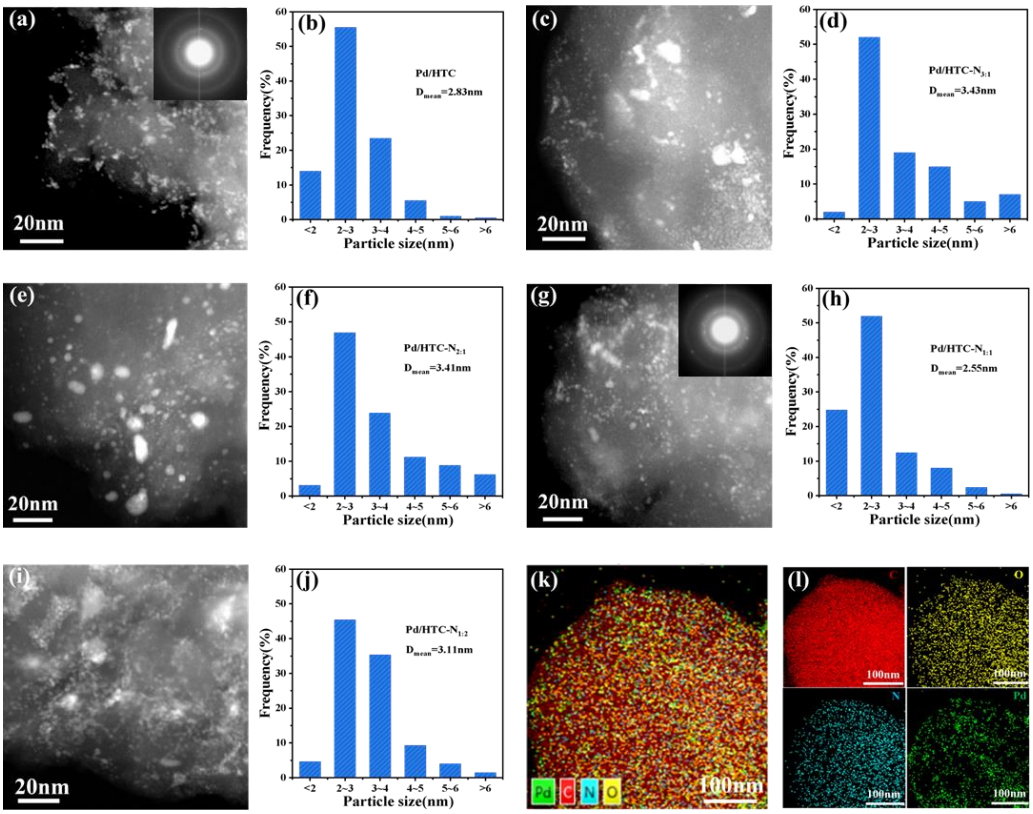

Figure 7. STEM images and the Pd particle size distributions of Pd/HTC (**a**,**b**), Pd/HTC-$N_{3:1}$ (**c**,**d**), Pd/HTC-$N_{2:1}$ (**e**,**f**), Pd/HTC-$N_{1:1}$ (**g**,**h**), and Pd/HTC-$N_{1:2}$ (**i**,**j**), and the elemental mapping of Pd/HTC-$N_{1:1}$ (**k**,**l**). Insets in (**a**,**g**) shows the corresponding SAED patterns.

The high resolution of Pd 3d and N 1s XPS spectra of Pd/HTC, Pd/HTC-$N_{3:1}$, Pd/HTC-$N_{2:1}$, Pd/HTC-$N_{1:1}$, and Pd/HTC-$N_{1:2}$ is shown in Figure 8. The Pd 3d signals could be fitted to three pairs of peaks represented with different colors. The Pd $3d_{3/2}$ peak at around 340.8 eV, 343.0 eV, 344.6 eV, and Pd $3d_{5/2}$ peak at about 335.7 eV, 337.7 eV, and 338.8 eV were assigned to Pd^0, PdO, and Pd^{2+} species, respectively [56,57]. A certain amount of Pd^{2+} ion existence reflected the strong interaction between Pd^{2+} and the carbon support. Considering no reducing agent existed in the preparation process, the presence of Pd^0 was possibly due to electron transfer between the Pd^{2+} and the carbon support. The ratio of Pd^0 species in the nitrogen-containing catalysts was much lower than that of the Pd/HTC sample (Table S3), suggesting that the coordination of Pd^{2+} to N-doped carbon made its reduction difficult [58]. The high PdO ratios demonstrated that PdO was the main form of Pd species on the catalysts (72.3–78.5%). Compared to Pd/HTC, the peak position of the PdO species on the nitrogen-containing samples moved to the low bonding energy range by 0.2–0.4 eV (Table S3). This is because the electron density of the N-doped carbon supports is higher than that of the N-free support, resulting in a reduction in the Pd oxidation state [59]. The ratios of total oxidized Pd species, PdO and Pd^{2+}, of the nitrogen-containing catalysts were in the order of Pd/HTC-$N_{1:1}$ > Pd/HTC-$N_{1:2}$ > Pd/HTC-$N_{2:1}$ > Pd/HTC-$N_{3:1}$, which was consistent with their activities in the debenzylation of TADB, implying that oxidic Pd species might be beneficial for the debenzylation reaction.

As presented in Figure 8b, three different components could be identified, centered at 398.7 eV, 400.3 eV, and 401.5 eV, corresponding to pyridinic N, pyrrolic N, and graphitic N, respectively [60]. It was known that the Pd nanoparticles can be strongly modified by the electronic effect of nitrogen-doped carbons, especially by the surface pyridinic N sites [61]. In the nitrogen-containing samples, the contents of pyridinic N (37.3–42.5%) were comparable to that of pyrrolic N (41.2–46.7%), while the graphitic N contents were relatively

low (15.0–18.3%) (Table S4). Among the four nitrogen-containing catalysts, Pd/HTC-$N_{1:1}$ had the highest pyridinic N content (42.5%). Combining the surface atomic contents of different catalysts (Table S2), one could find that the calculated surface pyridinic N contents of the nitrogen-containing samples were in the order of Pd/HTC-$N_{1:1}$ > Pd/HTC-$N_{1:2}$ > Pd/HTC-$N_{2:1}$ > Pd/HTC-$N_{3:1}$ (Table S5), which was consistent with their Pd dispersions as well as the activities in the hydrogenolysis reaction of TADB, implying that the surface pyridinic N content might be one reason dominating the Pd dispersion and activity. The high resolution of the O 1s and C 1s spectra (Figure S8, Tables S6 and S7) further revealed the existence of different oxygen-containing groups.

The above characterization results revealed that the Pd dispersion was the main reason that affected the debenzylation activity of the catalysts; meanwhile, the high total oxidized Pd species and high surface pyridinic N contents, as well as the eggshell distribution of the Pd species, were also beneficial to improve the catalyst activity. The high stability of Pd/HTC-$N_{1:1}$ was attributed to the relatively strong interaction between Pd and N atoms on the carbon matrix.

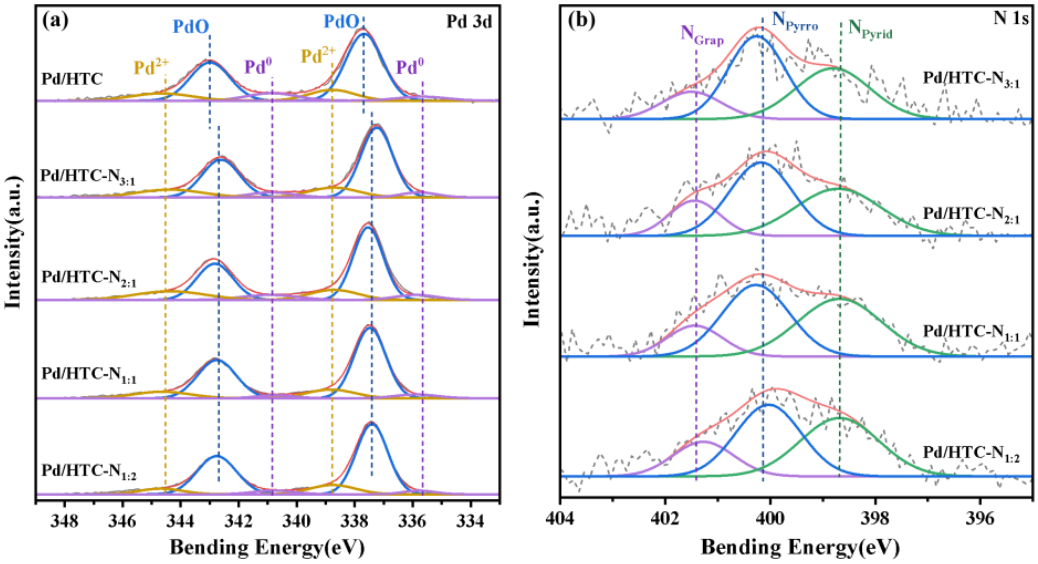

Figure 8. High resolution of Pd 3d (**a**) and N 1S (**b**) XPS spectra of the catalysts.

3. Materials and Methods

3.1. Chemicals

All chemicals were of an analytical grade and were used as received without a further purification. Microcrystalline cellulose (MC) was purchased from Beijing Enokai Technology Co., Ltd. (Beijing, China). Palladium chloride ($PdCl_2$, Pd 59.5 wt%) was purchased from Shanghai Jiuyue Chemical Co., Ltd. (Shanghai, China). Urea was purchased from Shanghai Meirell Chemical Technology Co., Ltd. (Shanghai, China). Glacial acetic acid (CH_3COOH) was purchased from Beijing Mairuida Technology Co., Ltd. (Beijing, China). Hydrochloric acid (HCl), perchloric acid ($HClO_4$), and acetic anhydride (AC_2O) were purchased from Beijing Yili Fine Chemical Co., Ltd. (Beijing, China). N,N-dimethylformamide (DMF) and bromobenzene (PhBr) were provided by Tianjin Fuchen Chemistry Co., Ltd. (Tianjin, China). Alcohol (C_2H_6O), sodium hydroxide (NaOH), and sodium bicarbonate ($NaHCO_3$) were purchased from Aladdin Chemistry Co., Ltd. (Shanghai, China). HBIW was an industrial product provided by the Qing Yang Chemical Industry Corporation (Liaoyang, China).

3.2. Synthesis of Carbon Supports

In a typical process, MC (13 g) was dissolved in 100 mL of deionized water, and then the suspension was poured into the Teflon-line stainless steel autoclave and heated at

220 °C for 24 h. After it was cooled to room temperature, the brown solid precipitate was recovered by filtration, washed with deionized water, and dried at 80 °C overnight. This brown solid was further calcinated at 700 °C for 2 h with the heating rate of 10 °C/min in a tube furnace under a N_2 atmosphere (100 mL/min). The received product was washed with 10 wt% HCl solution and deionized water and was dried at 80 °C for 12 h, providing the hydrothermal carbon sample, which was denoted as HTC. The nitrogen-containing carbon samples were prepared by a similar hydrothermal process in the presence of urea with the amounts of 4.3, 6.5, 13, and 26 g, respectively, and they were calcined under the same condition. According to the mass ratios of MC/urea, the resulting products were denoted as HTC-$N_{3:1}$, HTC-$N_{2:1}$, HTC-$N_{1:1}$, and HTC-$N_{1:2}$, respectively.

3.3. Catalysts Preparation

The $Pd(OH)_2/C$ was prepared trough a simple deposition–precipitation method (Scheme 2). In a typical preparation, a carbon carrier (2 g) was dispersed in 20 mL deionized water through vigorous stirring to form a carbon black suspension. Meanwhile, $PdCl_2$ (0.168 g) was dissolved in a 1 mL concentrated HCl solution and was diluted with 5 mL of deionized water to form homogeneous H_2PdCl_4 solution. Then, the H_2PdCl_4 solution was introduced to the carbon suspension. Under vigorously stirring, the NaOH solution (5 wt%) was added dropwise into the mixture until the system pH value increased up to 10. The slurry was filtered, washed extensively with deionized water until no chloride ion in the filtrate could be detected, and was dried at 60 °C overnight, providing the catalyst sample. All the catalysts were prepared under a similar condition, which were denoted as Pd/HTC, Pd/HTC-$N_{3:1}$, Pd/HTC-$N_{2:1}$, Pd/HTC-$N_{1:1}$, and Pd/HTC-$N_{1:2}$, respectively, according to the support names.

3.4. Catalytic Activity Tests

The debenzylation of HBIW was conducted under a condition reported by Wardle [12]. In a typical process, HBIW (20 g), catalyst (0.588 g), DMF (40 mL), AC_2O (20 mL), and PhBr (0.36 mL) were added into the reactor. Then, the reactor was immediately purged three times with hydrogen. The system was vigorously stirred under a H_2 atmosphere with 1 atm at room temperature until a small amount of solid product precipitated. Then, the system was heated to 43 °C and reacted continually for about 12 h. The TADB crude product was obtained by filtration and washed three times with alcohol (Figure S9). The yield was calculated using the following formula:

$$\text{Yield} = \frac{m_{TADB} - m_{Cat}}{m_{HBIW}} \times \frac{M_{HBIW}}{M_{TADB}} \times 100\%$$

where m_{Cat}, m_{TADB}, and m_{HBIW} are the mass of the catalyst, product TADB, and substrate HBIW, respectively, and M_{TADB} and M_{HBIW} are the molar mass of TADB and HBIW.

The debenzylation of TADB. The TADB crude product was used directly. In a typical process, TADB (20 g), catalyst (0.838 g), CH_3COOH (80 mL), perchloric acid (0.4 mL), and H_2O (20 mL) were added into the reactor. Then, the reactor was immediately purged three times with hydrogen. The system was vigorously stirred under H_2 with 1 atm at 43 °C for 12 h. After that, the catalyst was filtered, and the filtrate was concentrated under a vacuum. The resulting viscous material was washed with ethanol, providing a white solid product, hexanitrohexaazaisowurtzitane (TAIW). The cyclic experiments were performed under a similar condition as described above, in which the fresh catalyst (1.092 g) was added just in the first cycle, and reused after filtration.

3.5. Characterization and Instrumentation

The morphology and microstructure of the as-prepared material were characterized using scanning electron microscopy (SEM, JEOL JSM-35C) and scanning transmission electron microscopy (STEM, JEOL JEM-2010). The palladium particle sizes on STEM graphs were measured using the Nano Measurer software and the average particle sizes were

calculated according to the size data of 200 particles. Nitrogen adsorption–desorption isotherms were detected on a Micrometrics ASAP 2460 analyzer at 77 K. The surface area and pore size distribution were determined using the Brunauer–Emmett–Teller (BET) method and the Barrett–Joyner–Halenda (BJH) method, respectively. Prior to the measurements, the sample (about 100 mg) was degassed under a vacuum at 150 °C for 6 h. The powder X-ray diffraction was conducted on a Bruker/AXS D8 Advance instrument operating at 40 kV and 40 mA using Cu Kα radiation (λ = 1.5406 Å). The samples were scanned from 10° to 80° (2θ) with the scanning step size of 0.02°. The X-ray photoelectron spectroscopy (XPS) studies were finished on Thermo Scientific K-Alpha equipment with Al Kα ($h\nu$ = 1486.6 eV) as the excitation source, and the binding energy data of all the catalysts were determined using the C1s binding energy (284.8 eV) as a calibration. Raman spectra were received on a Horiba LabRAM HR Evolution using the excitation wavelength of 532 nm. The temperature-programmed desorption (TPD) spectra were performed on a platform combining a chemisorbent analyzer (Micromeritics, AutoChem II 2920) with a mass spectrometer (HIDEN QGA). For each experiment, about 50–100 mg of sample was loaded into a U-shaped tube, purged with He gas (40 mL/min) at room temperature, and preprocessed at 120 °C for 30 min with a heating rate of 10 °C/min under the disconnection of a mass spectrometer. After that, the mass spectrometer was turned on, and the sample was continued to be purged with He gas (40 mL/min) at room temperature for 60 min until the baseline remained unchanged, and then the sample was heated at a programmed temperature range of 20–900 °C with a heating rate of 10 °C/min. The desorbed CO and CO_2 were measured online using a HIDEN QGA mass spectrometer to obtain the CO-TPD and CO_2-TPD spectral lines. The products (TADB and TAIW) were analyzed using Agilent Technologies 6100 high-performance liquid chromatography (HPLC). The sample was dissolved in acetonitrile, followed by filtration to remove particulates. The mobile phase was 75% methanol in water at a 0.8 mL/min flow rate, and a UV/vis detector operating at 230 nm was employed. The chemical structure of TADB and TAIW were determined by ^{1}H-NMR using Bruker ARX-400 spectrometers with DMSO solution and D_2O solution, respectively, using tetramethylsilane as an internal standard (Figures S10 and S11).

4. Conclusions

In summary, a series of $Pd(OH)_2/C$ catalysts using microcrystalline cellulose-derived carbon as supports were fabricated. The effects of the nitrogen doping on the carbon support structures as well as the activities of the corresponding catalysts in the debenzylation reaction of HBIW and TADB were investigated. It was found that the carbon structure changed significantly, including the decreases in the specific surface area and the changes in the pore structure and surface-oxygen-containing and nitrogen-containing groups' concentrations due to the nitrogen introduction. All the nitrogen-containing and nitrogen-free catalysts showed high activities in the debenzylation of HBIW, revealing that the structure of the resulting carbon supports had a limited impact on the catalyst performance in this reaction, while the activities of various catalysts in the debenzylation of TADB were quite different. Among them, Pd/HTC-$N_{1:1}$ showed a much higher activity compared to the reported catalysts. The relatively high activity of Pd/HTC was related to the high Pd dispersion and novel mesoporous structure. The further high activity and stability of Pd/HTC-$N_{1:1}$ was associated with its high Pd dispersion, high total oxidized Pd species, and high surface pyridinic N contents, as well as the eggshell distribution of the Pd species on the support. The result was useful to reduce the consumption of precious metal palladium in the debenzylation reaction so as to decrease the production cost of CL-20.

Supplementary Materials: The following supporting information can be downloaded at: https://www.mdpi.com/article/10.3390/catal13030637/s1, Figure S1: N_2 absorption–desorption isotherms and pore-size distribution curves; Figure S2: XRD patterns of the carbon supports; Figure S3: Raman spectra of the carbon supports; Figure S4: TEM bright field image of Pd/HTC-$N_{1:1}$; Figure S5: SEM images of the recovered Pd/HTC (a) and Pd/HTC-N1:1 (b) samples; Figure S6: STEM images and the Pd particle size distributions of Pd/HTC and Pd/HTC-$N_{1:1}$ after three cycles; Figure S7: XPS survey spectrum of various catalysts; Figure S8: High resolution of O 1s and C 1s XPS spectra of the catalysts; Figure S9: HPLC data of TADB crude product; Figure S10: ^{1}H-NMR figure of TADB in D_2O; Figure S11: ^{1}H-NMR figure of TAIW in D_2O; Table S1: Activities of Pd/HTC and Pd/HTC-$N_{1:1}$ in the three cycles of TADB debenzylation; Table S2: Surface atomic contents of different catalysts; Table S3: XPS binding energies of Pd species and the ratios in different catalysts; Table S4: XPS binding energies of N species and the ratios in different catalysts; Table S5: Calculated surface pyridinic N contents and surface pyridinic N/Pd molar ratios; Table S6: Surface atomic concentrations of the oxygen species of various catalysts; Table S7: Surface atomic concentrations of the carbon species of various catalysts.

Author Contributions: Conceptualization, W.Q. and J.S.; methodology, Y.W. and W.Q.; validation, Y.W. and Y.C.; formal analysis, Y.W., Y.C., H.D. and X.D.; investigation, Y.W., X.D., H.W., Y.L. and W.Q.; resources, W.Q.; data curation, Y.W., G.W. and W.Q.; writing original draft preparation, Y.W.; writing review and editing, W.Q.; visualization, Y.W. and W.Q.; supervision, W.Q., J.S. and G.B.; project administration, W.Q., G.W. and G.B.; funding acquisition, W.Q. All authors have read and agreed to the published version of the manuscript.

Funding: This research was funded by the National Natural Science Foundation of China (No. 22075005).

Data Availability Statement: Not applicable.

Conflicts of Interest: The authors declare no conflict of interest.

References

1. Theodoridis, G. Nitrogen protecting groups: Recent developments and new applications. *Tetrahedron* **2000**, *56*, 2339–2358. [CrossRef]
2. Lange, S.; Formenti, D.; Lund, H.; Kreyenschulte, C.R.; Agostini, G. Additive-free nickel-catalysed debenzylation reactions via hydrogenative C-O and C-N bond cleavage. *ACS Sustain. Chem. Eng.* **2019**, *7*, 17107–17113. [CrossRef]
3. Sandee, A.J.; Chintada, T.J.; Groen, C.; Donkervoort, J.G.; Terorde, R.J.A.M. Optimized palladium on activated carbon formulation for N-hydrogenolysis reactions. *Chim. Oggi-Chem. Today* **2013**, *31*, 20–23.
4. Mao, J.F.; Gregory, D.H. Recent advances in the use of sodium borohydride as a solid state hydrogen store. *Energies* **2015**, *8*, 430–453. [CrossRef]
5. Ram, S.; Spicer, L.D. Debenzylation of N-benzylamino derivatives by catalytic transfer hydrtyation with ammonium formate. *Synth. Commun.* **1987**, *17*, 415–418. [CrossRef]
6. Watanabe, T.; Kobayashi, A.; Nishiura, M.; Takahashi, H.; Usui, T.; Kamiyama, I. Synthetic studies on indoles and related-compounds. 26. The debenzylation of protected indole nitrogen with aluminum-chloride. *Chem. Pharm. Bull.* **1991**, *39*, 1152–1156. [CrossRef]
7. Rombouts, F.; Franken, D.; Martínez-Lamenca, C. Microwave-assisted N-debenzylation of amides with triflic acid. *Tetrahedron Lett.* **2010**, *51*, 4815–4818. [CrossRef]
8. Kovacs, E.; Thurner, A.; Farkas, F. Hydrogenolysis of N-protected aminooxetanes over palladium: An efficient method for a one-step ring opening and debenzylation reaction. *J. Mol. Catal. A Chem.* **2011**, *339*, 32–36. [CrossRef]
9. Nielsen, A.T.; Nissan, R.A.; Vanderah, D.J. Polyazapolycyclics by condensation of aldehydes with amines. 2. Formation of 2,4,6,8,10,12-hexabenzyl-2,4,6,8,10,12-hexaazatetracyclo[5.5.0.$0^{5,9}$.$0^{3,11}$]dodecanes from glyoxal and benzylamines. *J. Org. Chem.* **1990**, *55*, 1459–1466. [CrossRef]
10. Bellamy, A.J. Reductive debenzylation of hexabenzylhexaazaisowurtzitane. *Tetrahedron* **1995**, *51*, 4711–4722. [CrossRef]
11. Nielsen, A.T.; Chafin, A.P.; Christian, S.L. Synthesis of polyazapolycyclic caged polynitramines. *Tetrahedron* **1998**, *54*, 11793–11812. [CrossRef]
12. Wardle, R.B. Improved Hydrogenolysis of 2,4,6,8,10,12-Hexabenzyl-2,4,6,8,10,12-Hexaazatetracyclo [5.5.0.$0^{5,9}$.$0^{3,11}$] Dodecane. U.S. Patent 5,739,325, 14 April 1998.
13. Yu, Y.Z.; Guan, X.P. Studies on the synthesis of hexanitrohexaazaisowurtzitane. *Chin. J. Energetic Mater.* **1999**, *7*, 1–4.
14. Zheng, F.P.; Ou, Y.X.; Chen, J.T. The preparation and characterization of nanosized $Pd(OH)_2$ and its application in the catalytic hydrogenolysis of HBIW. *Chem. J. Chin. Univ.* **1999**, *20*, 843–845.

15. Koskin, A.P.; Simakova, I.L.; Parmon, V.N. Study of palladium catalyst deactivation in synthesis of 4,10-diformyl-2,6,8,12-tetraacetyl-2,4,6,8,10,12-hexaazaisowurtzitane. *React. Kinet. Catal. Lett.* **2007**, *92*, 293–302. [CrossRef]
16. Zhang, M.X.; Liu, S.; Li, L. Effect of carbon supports on Pd catalyst for hydrogenation debenzylation of hexabenzylhexaazaisowurtzitane (HBIW). *J. Energ. Mater.* **2017**, *35*, 251–264. [CrossRef]
17. Koskin, A.P.; Simakova, I.L.; Parmon, V.N. Reductive debenzylation of hexabenzylhexaazaisowurtzitane—The key step of the synthesis of polycyclic nitramine hexanitrohexaazaisowurtzitane. *Russ. Chem. Bull. Int. Ed.* **2007**, *56*, 2370–2375. [CrossRef]
18. Qiu, W.G.; Liu, H.B.; Dong, K. Preparation of $Pd(OH)_2/C$ catalyst for hydrogenolytic debenzylation of hexabenzylhexaazaisowurtzitane. *Chin. J. Energ. Mater.* **2014**, *22*, 441–446.
19. Maksimowski, P.; Golofit, T.; Tomaszewski, W. Palladium catalyst in the HBIW hydrodebenzylation reaction. Deactivation and spent catalyst regeneration procedure. *Cent. Eur. J. Energetic Mater.* **2016**, *13*, 333–348. [CrossRef] [PubMed]
20. Fotouhi-Far, F.; Bashiri, H.; Hamadanian, M. Study of deactivation of $Pd(OH)_2/C$ catalyst in reductive debenzylation of hexabenzylhexaazaisowurtzitane. *Propellants Explos. Pyrotech.* **2017**, *42*, 213–219. [CrossRef]
21. Chen, Y.; Qiu, W.G.; Sun, J.Y. Synthesis of flowerlike carbon nanosheets from hydrothermally carbonized glucose: An in situ selfgenerating template strategy. *RSC Adv.* **2019**, *9*, 37355–37364. [CrossRef]
22. Nan, J.P.; Wang, Y.L.; Song, J.W.; Qiu, W.G. Effects of the preparation condition of carbon support on the hydrogenolytic debenzylation performance of the corresponding $Pd(OH)_2/C$ catalysts. *Chin. J. Energetic Mater.* **2022**, *30*, 1138–1146.
23. Zhang, Q.F.; Wang, M.; Qian, J.C.; Lou, S.Y.; Jin, J.H.; Li, B.C.; Lu, C.S.; Feng, F.; Lv, J.H.; Wang, Q.T.; et al. Deactivation and regeneration of palladium catalysts for hydrogenation debenzylation of 2,4,6,8,10,12-hexabenzyl-2,4,6,8,10,12-hexaazaisowurtzitane (HBIW). *Catalysts* **2022**, *12*, 1547. [CrossRef]
24. Liu, S.; Ji, F.; Li, X.Y. Stick-like mesoporous titania loaded Pd as highly active and cost effective catalysts for hydrodebenzylation of hexabenzylhexaazaisowurtzitane (HBIW). *Mol. Catal.* **2019**, *477*, 110556. [CrossRef]
25. Zhao, W.; Liu, S.; Wang, H.S. Ultrasmall Pd nanoparticles supported on TiO_2 for catalytic debenzylation via hydrogenative C-N bond cleavage. *ACS Appl. Nano Mater.* **2021**, *4*, 159–166. [CrossRef]
26. Dong, K.; Chen, Y.; Zhang, Y.Y. The highly effective hydrogenolysis-based debenzylation of tetraacetyldibenzylhexaazaisowurtzitane (TADBIW) using a Palladium/DOWEX catalyst having a synergistic effect. *J. Energ. Mater.* **2017**, *35*, 421–429.
27. Liu, W.; Li, S.F.; She, C.C. Excellent stability of Pd/mpg-C_3N_4 in catalytic hydrodebenzylation of 2, 4, 6,8,10,12-hexabenzy1-2,4,6,8,10,12-hexaazaisowurtzitane (HBIW). *Appl. Catal. A-Gen.* **2021**, *624*, 118310. [CrossRef]
28. Lou, D.Y.; Wang, H.S.; Liu, S. PdFe bimetallic catalysts for debenzylation of hexabenzylhexaazaisowurtzitane (HBIW) and tetraacetyldibenzylhexaazaisowurtzitane (TADBIW). *Catal. Commun.* **2018**, *109*, 28–32. [CrossRef]
29. Chen, S.Y.; Liu, S.; Men, Y. Synergistic catalysis of PdFe bimetallic nanoparticles supported on SiO_2 for hydrogenative cleavage of C-N bonds. *ACS Appl. Nano Mater.* **2021**, *4*, 6020–6029. [CrossRef]
30. Cabiac, A.; Delahay, G.; Durand, R. The influence of textural and structural properties of Pd/carbon on the hydrogenation of cis,trans,trans-1,5,9-cyclododecatriene. *Appl. Catal. A-Gen.* **2007**, *318*, 17–21. [CrossRef]
31. Cabiac, A.; Cacciaguerra, T.; Trens, P. Influence of textural properties of activated carbons on Pd/carbon catalysts synthesis for cinnamaldehyde hydrogenation. *Appl. Catal. A-Gen.* **2008**, *340*, 229–235. [CrossRef]
32. Jain, A.; Balasubramanian, R.; Srinivasan, M.P. Hydrothermal conversion of biomass waste to activated carbon with high porosity: A review. *Chem. Eng. J.* **2016**, *283*, 789–805. [CrossRef]
33. Lam, E.; Luong, J.H.T. Carbon materials as catalyst supports and catalysts in the transformation of biomass to fuels and chemicals. *ACS Catal.* **2014**, *4*, 3393–3410. [CrossRef]
34. Sevilla, M.; Fuertes, A.B. The production of carbon materials by hydrothermal carbonization of cellulose. *Carbon* **2009**, *47*, 2281–2289. [CrossRef]
35. Wu, X.Y.; Tang, J.T.; Duan, Y.C. Conductive cellulose nanocrystals with high cycling stability for supercapacitor applications. *J. Mater. Chem. A* **2014**, *2*, 19268–19274. [CrossRef]
36. Yi, X.T.; Liu, C.; Liu, X.K. Magnetic partially carbonized cellulose nanocrystal-based magnetic solid phase extraction for the analysis of triazine and triazole pesticides in water. *Microchim. Acta* **2019**, *186*, 825. [CrossRef] [PubMed]
37. Hamedi, M.; Karabulut, E.; Marais, A. Nanocellulose aerogels functionalized by rapid layer-by-layer assembly for high charge storage and beyond. *Angew. Chem.-Int. Ed.* **2013**, *52*, 12038–12042. [CrossRef] [PubMed]
38. Xu, X.Z.; Zhou, J.; Nagaraju, D.H. Flexible, highly graphitized carbon aerogels based on bacterial cellulose/lignin: Catalyst-free synthesis and its application in energy storage devices. *Adv. Funct. Mater.* **2015**, *25*, 3193–3202. [CrossRef]
39. Jiang, Y.T.; Yan, J.; Wu, X.L. Facile synthesis of carbon nanofibers-bridged porous carbon nanosheets for high-performance supercapacitors. *J. Power Source* **2016**, *307*, 190–198. [CrossRef]
40. Lu, H.; Sun, X.M.; Gaddam, R.R. Electrocapacitive properties of nitrogen-containing porous carbon derived from cellulose. *J. Power Source* **2017**, *360*, 634–641. [CrossRef]
41. Lu, H.; Zhuang, L.Z.; Gaddam, R.R. Microcrystalline cellulose-derived porous carbons with defective sites for electrochemical applications. *J. Mater. Chem. A* **2019**, *7*, 22579–22587. [CrossRef]
42. Paksung, N.; Pfersich, J.; Arauzo, P.J. Structural effects of cellulose on hydrolysis and carbonization behavior during hydrothermal treatment. *ACS Omega* **2020**, *5*, 12210–12223. [CrossRef] [PubMed]
43. Mao, D.L.; Qiu, J.H.; Jia, M.M. Platinum supported cellulose-based carbon with oxygen-containing functional groups for benzyl alcohol oxidation. *J. Phys. Chem. Solids* **2019**, *135*, 109095. [CrossRef]

44. Xia, J.Q.; Cheng, M.; Hu, J. $Zn_5(OH)_6(CO_3)_2$-assisted controlled fabrication of microcrystalline cellulose-derived hierarchical porous carbon for high-performance lithium storage. *J. Alloys Compd.* **2022**, *911*, 165131. [CrossRef]
45. Wu, X.S.; Dong, X.L.; Wang, B.Y. Revealing the sodium storage behavior of biomass-derived hard carbon by using pure lignin and cellulose as model precursors. *Renew. Energy* **2022**, *189*, 630–638. [CrossRef]
46. Garba, Z.N.; Lawan, I.; Zhou, W.M. Microcrystalline cellulose (MCC) based materials as emerging adsorbents for the removal of dyes and heavy metals—A review. *Sci. Total Environ.* **2020**, *717*, 135070. [CrossRef]
47. Fuertes, A.B.; Arbestain, M.C.; Sevilla, M. Chemical and structural properties of carbonaceous products obtained by pyrolysis and hydrothermal carbonisation of corn stover. *Aust. J. Soil Res.* **2010**, *48*, 618–626. [CrossRef]
48. Kang, S.M.; Li, X.L.; Fan, J. Characterization of hydrochars produced by hydrothermal carbonization of lignin, cellulose, D-xylose, and wood meal. *Ind. Eng. Chem. Res.* **2012**, *51*, 9023–9031. [CrossRef]
49. Huang, T.; Wu, Z.C.; Yu, Q. Preparation of hierarchically porous carbon/magnetic particle composites with broad microwave absorption bandwidth. *Chem. Eng. J.* **2019**, *359*, 69–78. [CrossRef]
50. Deng, X.; Zhao, B.T.; Zhu, L.; Shao, Z.P. Molten salt synthesis of nitrogen-doped carbon with hierarchical pore structures for use as high-performance electrodes in supercapacitors. *Carbon* **2015**, *93*, 48–58. [CrossRef]
51. Abakumov, A.A.; Bychko, I.B.; Selyshchev, O.V. Catalytic properties of reduced graphene oxide in acetylene hydrogenation. *Carbon* **2020**, *157*, 277–285. [CrossRef]
52. Sadezky, A.; Muckenhuber, H.; Grothe, H. Raman micro spectroscopy of soot and related carbonaceous materials: Spectral analysis and structural information. *Carbon* **2005**, *43*, 1731–1742. [CrossRef]
53. Aksoylu, A.E.; Madalena, M.; Freitas, A. The effects of different activated carbon supports and support modifications on the properties of Pt/AC catalysts. *Carbon* **2001**, *39*, 175–185. [CrossRef]
54. Zhou, J.H.; Sui, Z.J.; Zhu, J. Characterization of surface oxygen complexes on carbon nanofibers by TPD, XPS and FT-IR. *Carbon* **2007**, *45*, 785–796. [CrossRef]
55. Cabiac, A.; Delahay, G.; Durand, R. Controlled preparation of Pd/AC catalysts for hydrogenation reactions. *Carbon* **2007**, *45*, 3–10. [CrossRef]
56. An, N.H.; Dai, Y.S.; Tang, C. Design and preparation of a simple and effective palladium catalyst and the hydrogenation performance toward dibenzylbiotinmethylester. *J. Colloid Interface Sci.* **2016**, *470*, 56–61. [CrossRef]
57. Zhang, C.; Fan, L.M.; Ren, J.J. Facile synthesis of surface functionalized Pd^{2+}@P-CDP/COFs for highly sensitive detection of norfloxacin drug based on the host-guest interaction. *J. Pharm. Biomed. Anal.* **2022**, *219*, 114956. [CrossRef] [PubMed]
58. Arrigo, R.; Schuster, M.E.; Xie, Z.L. Nature of the N-Pd interaction in nitrogen-doped carbon nanotube catalysts. *ACS Catal.* **2015**, *5*, 2740–2753. [CrossRef]
59. Koh, K.; Seo, J.E.; Lee, J.H. Ultrasmall palladium nanoparticles supported on amine-functionalized SBA-15 efficiently catalyze hydrogen evolution from formic acid. *J. Mater. Chem. A* **2014**, *2*, 20444–20449. [CrossRef]
60. Abate, S.; Arrigo, R.; Schuster, M.E. Pd nanoparticles supported on N-doped nanocarbon for the direct synthesis of H_2O_2 from H_2 and O_2. *Catal. Today* **2010**, *157*, 280–285. [CrossRef]
61. Kim, Y.; Kim, D.H. Hydrogen production from formic acid dehydrogenation over a Pd supported on N-doped mesoporous carbon catalyst: A role of nitrogen dopant. *Appl. Catal. A-Gen.* **2020**, *608*, 117887. [CrossRef]